



Evershed and Counter-Evershed Flows in Sunspot MHD Simulations

A. L. Siu-Tapia^{1,2} , M. Rempel³ , A. Lagg¹ , and S. K. Solanki^{1,4} 

¹Max-Planck-Institut für Sonnensystemforschung, Justus-von-Liebig-Weg 3, D-37077 Göttingen, Germany

²Universität Göttingen, Physikalisches Institut, Friedrich-Hund-Platz 1, D-37077 Göttingen, Germany

³High Altitude Observatory, NCAR, P.O. Box 3000, Boulder, CO 80307, USA

⁴School of Space Research, Kyung Hee University, Yongin, 446-701 Gyeonggi, Republic of Korea

Received 2017 September 11; revised 2017 November 27; accepted 2017 December 4; published 2018 January 8

Abstract

There have been a few reports in the literature of counter-Evershed flows observed in well-developed sunspot penumbrae, i.e., flows directed toward the umbra along penumbral filaments. Here, we investigate the driving forces of such counter-Evershed flows in a radiative magnetohydrodynamic simulation of a sunspot, and compare them to the forces acting on the normal Evershed flow. The simulation covers a timespan of 100 solar hours and generates an Evershed outflow exceeding 8 km s^{-1} in the penumbra along radially aligned filaments where the magnetic field is almost horizontal. Additionally, the simulation produces a fast counter-Evershed flow (i.e., an inflow near $\tau = 1$) in some regions within the penumbra, reaching peak flow speeds of $\sim 12 \text{ km s}^{-1}$. The counter-Evershed flows are transient and typically last a few hours before they turn into outflows again. By using the kinetic energy equation and evaluating its various terms in the simulation box, we found that the Evershed flow occurs due to overturning convection in a strongly inclined magnetic field, while the counter-Evershed flows can be well-described as siphon flows.

Key words: Sun: magnetic fields – Sun: photosphere – sunspots

1. Introduction

The origin of large-scale flows in the penumbra of sunspots is of particular interest in observational and theoretical studies of sunspots. The most prominent flow in photospheric penumbrae is the Evershed flow (EF; Evershed 1909), an almost horizontal flow of plasma directed radially outward with speeds in the range of kilometers per second (typical spatially averaged speeds being $1\text{--}2 \text{ km s}^{-1}$). The nearly horizontal flow is usually subsonic, although supersonic flows have been observed (e.g., Wiehr 1995; del Toro Iniesta et al. 2001; Bellot Rubio et al. 2004; Borrero et al. 2005). The physical mechanism responsible for driving the EF is closely connected to the fine structure of the penumbra, which is manifested through the penumbral intensity, magnetic field, and velocity structure (see, e.g., detailed reviews by Solanki 2003; Thomas & Weiss 2004, 2008; Borrero 2009; Scharmer 2009; Schlichenmaier 2009; Tritschler 2009; Bellot Rubio 2010; Borrero & Ichimoto 2011; Rempel & Schlichenmaier 2011). All these quantities display an almost radial filamentary structure in the penumbra. In particular, the magnetic field configuration comprises two major components: the first contains generally stronger and more vertical fields (so-called spines), and is thought to be the result of a protrusion of the umbral field into the penumbra (see, e.g., review by Borrero & Ichimoto 2011); the second one is composed of weaker and more inclined fields (intra-spines, hereafter referred to as filaments) where the EF takes place (see, e.g., Tiwari et al. 2013). This configuration has been referred to as *uncombed penumbra* (Solanki & Montavon 1993) or *interlocking-comb structure* (Thomas & Weiss 1992).

Several models have been proposed to explain the filamentary nature of the penumbra, e.g., Danielson (1961), Meyer & Schmidt (1968), Choudhuri (1986), Solanki & Montavon (1993), Schlichenmaier et al. (1998a, 1998b), Thomas et al. (2002), Spruit & Scharmer (2006), Scharmer & Spruit (2006). However, not all the models contain a

self-consistent description of the EF. Some models based on stationary magnetic flux tubes representing the filaments describe the EF as a siphon flow driven by a gas pressure difference between the footpoints of the flux tube (e.g., Thomas & Montesinos 1993). On the other hand, the dynamic magnetic flux tube model presented by Schlichenmaier et al. (1998a) produces an EF as a combination of hot plasma rising at the inner footpoint of the tube and a radial acceleration driven by a pressure gradient, as a consequence of radiative losses at the surface. There is also the model of Scharmer & Spruit (2006), which says that the EF takes place in field-free intrusions. More recently, numerical magnetohydrodynamics (MHD) simulations have succeeded in reproducing the EF as a result of overturning convection in the presence of an inclined magnetic field (e.g., Heinemann et al. 2007; Scharmer et al. 2008; Kitiashvili et al. 2009; Rempel et al. 2009a, 2009b; Rempel 2011, 2012). The EF, in these cases, is interpreted as the convective flow component in the direction of the magnetic field. In these models, the penumbral fine structure results from anisotropic magneto-convection.

During the early stages of penumbrae formation, line-of-sight velocities with a sign opposite to that displayed by the typical EF have been reported by Schlichenmaier et al. (2012) and Romano et al. (2014). These have been interpreted as inflows toward the pore before the formation of the penumbra. On rare occasions, well-developed penumbrae can also harbor counter-EF (inflows) at the photosphere (Kleint & Sainz Dalda 2013; Louis et al. 2014; Siu-Tapia et al. 2017). In particular, Siu-Tapia et al. (2017) reported the observation of a prominent counter-EF with a lifetime of ~ 2 days in the disk center-side of a well-developed penumbra. The counter-EF showed considerable fine structure, i.e., the counter-EF was confined along “reversed” penumbral filaments, with their heads/sources located at the outer penumbral boundary and their tails/sinks observed at the inner penumbral edge. Siu-Tapia et al. (2017) showed that, as in the normal-EF, the

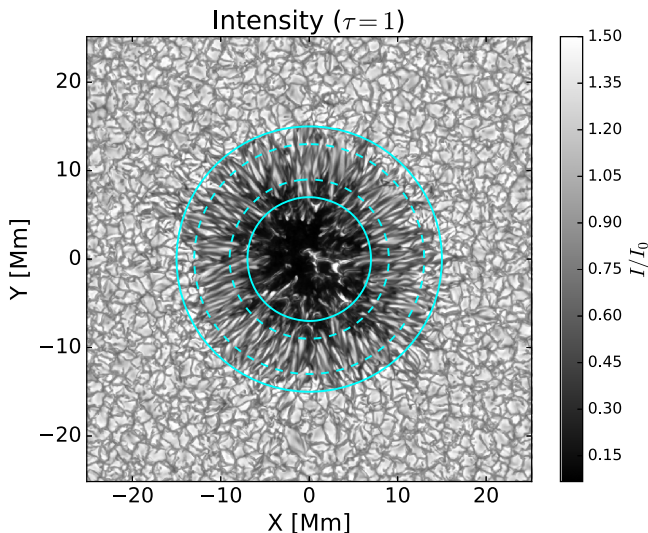


Figure 1. Intensity image of the simulated sunspot, relative to the average quiet Sun intensity I_0 , at about 67 hr after initialization of the simulation run. The image corresponds to the full spatial resolution series and shows the innermost $50.2 \times 50.2 \text{ Mm}^2$ of the simulation domain. Solid circles have been placed at radial distances of 7 Mm (where the azimuthally averaged intensity reaches $0.45I_0$) and 15 Mm (where the azimuthally averaged intensity reaches $0.9I_0$) from the center of the sunspot, delimiting the inner and outer penumbra, respectively. The dashed circles at $R = 9$ and 13 Mm delimit the middle penumbra.

filaments carrying the counter-EF display temperature and magnetic field gradients that are both consistent with the direction of the flow, being compatible with both the magneto-convective driver scenario as well as the siphon flow mechanism.

In this work, we analyze the results of an MHD high-resolution sunspot simulation by Rempel (2015), which produces a penumbra with normal-EF (outflows) as well as a fast counter-EF (inflows) in some parts of the penumbra at photospheric heights, with lifetimes of several hours. We investigate and identify the driving forces acting on both the normal EF and counter-EF.

2. Simulation

We analyze the 3D high-resolution sunspot simulation setup described in detail by Rempel (2015) and used therein to study the role of the penumbra and associated flows for sunspot decay. The simulation is based on the MURaM radiative MHD code (Vögler et al. 2005; Rempel et al. 2009b; Rempel 2014) and covers a timespan of 100 solar hours. An animation covering 25 hr (from $t = 50$ to 75 hr after the initialization of the simulation) is provided as part of the online material for Rempel (2015).

As described in Rempel (2015), the sunspot setup used open boundary conditions that do not maintain the initial field structure against decay driven by convective motions. The simulation’s initial state was a relaxed, small-scale dynamo. The sunspot simulation was then initialized by inserting an axisymmetric, self-similar magnetic field structure into the domain, with total initial flux of $9 \times 10^{21} \text{ Mx}$ and a field strength of $\sim 20 \text{ kG}$ at the bottom of the domain and $\sim 3 \text{ kG}$ at the top of the domain. The simulated sunspot had an almost constant magnetic flux for the simulated timespan of 100 hr,

and used a magnetic top boundary condition that imposes a sufficiently horizontal field to maintain a penumbra.

After $t = 50$ hr, the simulated sunspot showed well-developed penumbral fine structure (see, e.g., Figure 1 for an intensity image obtained about 67 solar hours after initialization of the simulation), i.e., it has radially aligned filaments with a close-to-horizontal field (see Figure 2). Along these filaments, there are fast radial outflows reaching peak flow velocities of $\sim 12 \text{ km s}^{-1}$. In addition to these outflow regions, there are also some patches in the penumbra that have a counter-EF (inflows in the photosphere). These regions are transient, only lasting a few hours before they turn into outflows again.

To investigate the nature of the counter-EF, we analyze the simulation time-steps from 60 to 70 solar hours (the range of time during which the counter-EF are found in the simulations). As described in Rempel (2015), the photosphere is located about 700 km beneath the top boundary, and the simulation domain extends about 18 Mm in depth below the photosphere and 98 Mm horizontally, using a grid spacing of 24 km vertically and 48 km horizontally, which is required to capture penumbral fine structure and the Evershed flow. The simulation ran on a $2048 \times 2048 \times 768 \text{ xyz}$ -grid (in the following presentation, the z -direction is vertical). Full-resolution data cubes were written every 4500 s, whereas data cubes at half the spatial resolution were written every 900 s. A non-gray run was restarted from one of the full-resolution cubes and evolved for 5000 time steps, i.e., 1125 s. All of the snapshots have improved numerics to address the drift problem described in Rempel (2015), which is related to numerical diffusion and the need for $\nabla \cdot B$ cleaning.

A full spatial resolution snapshot obtained with non-gray radiative transfer ($t \sim 67$ solar hours) is used in this work to study the filamentary structure of the normal EF and counter-EF. The half-resolution data cubes obtained with gray radiative transfer are employed to analyze the driving of the flows in the penumbra and their evolution in time.

3. Results

3.1. Filamentary Structure of the Penumbra

Figure 1 shows the normalized intensity of the simulated sunspot at $\tau = 1$ for a snapshot at $t \sim 67$ solar hours. Here, we are mainly interested in the penumbra, which appears to have a uniform filamentary structure in intensity at $\tau = 1$.

Figure 2 displays the filamentary fine structure of the penumbra as seen in the different physical quantities and at different optical depths: $\log(\tau) = -4, -2, -0.8$, and 0. The filamentary structure of the penumbra is more evident at $\log(\tau) = 0$, where the penumbral filaments appear as bright (hot) elongated channels with magnetic fields that become more inclined from the inner penumbral edge outward, and return back to the interior ($\gamma > 90^\circ$) toward the outer penumbral edge. Also, the velocity vector in the penumbral filaments is mostly radial.

The radial velocity maps in Figure 2 (fourth row) show that the penumbra is dominated by an inflow with respect to the center of the spot (red-to-yellow colors) at $\log(\tau) = -4.0$, which resembles the chromospheric *inverse* Evershed flow (IEF) (Dialexis et al. 1985) but occurs at lower heights, and by an outflow below $\log(\tau) = -2.0$ (blue-to-black colors), which represents the photospheric normal EF. However, there are also

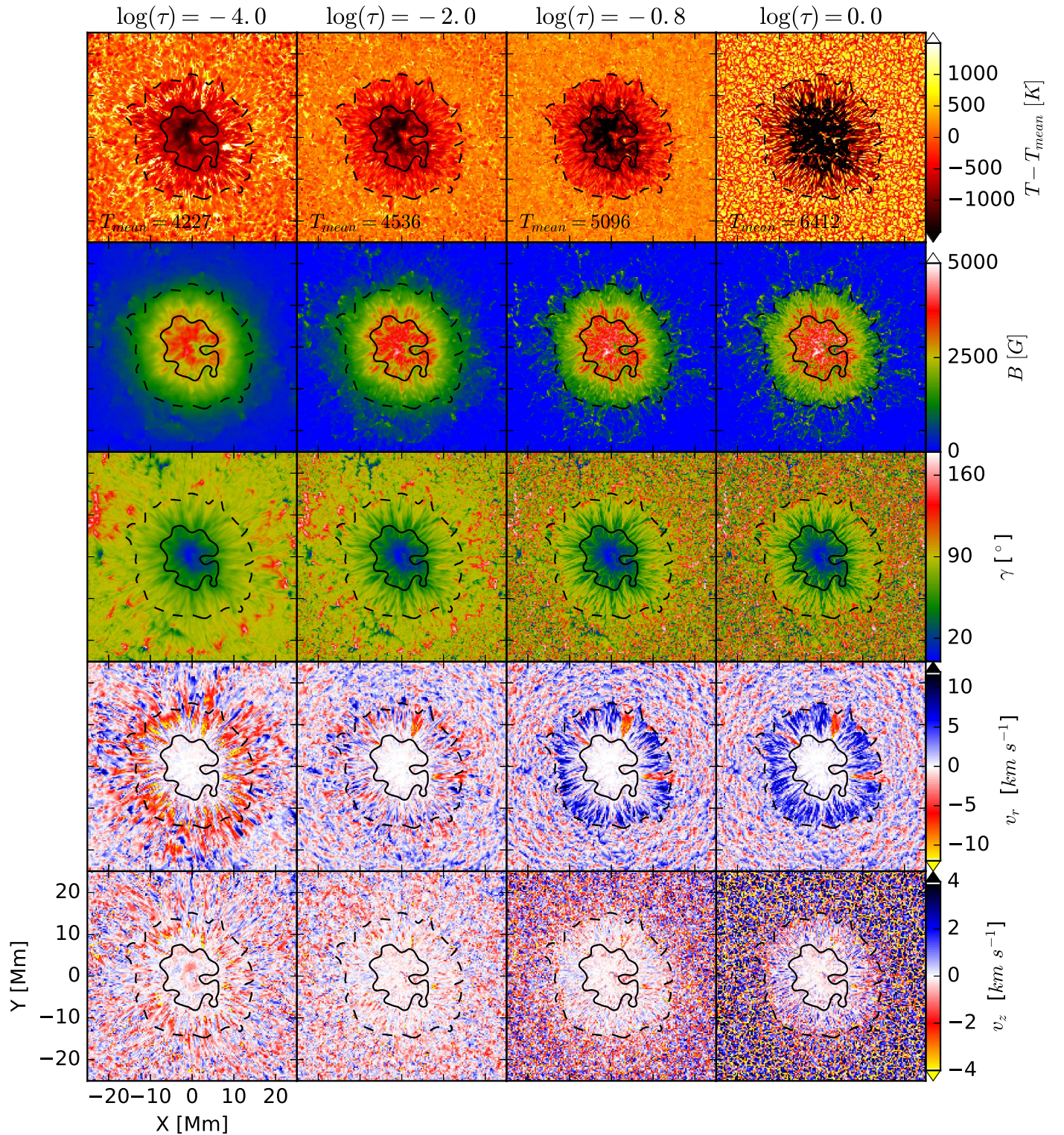


Figure 2. Fine structure of the sunspot at different optical depth levels. From left to right: $\log(\tau) = -4$, -2 , -0.8 , and 0 . From top to bottom: temperature perturbation, $T - T_{\text{mean}}$ [K]; magnetic field strength, B [G]; field inclination, γ [$^\circ$] with respect to vertical; radial flow velocity, v_r [km s^{-1}]; and vertical flow velocity, v_z [km s^{-1}]. A field inclination of 0° corresponds to a vertical field with the same polarity as the umbra, 90° to the horizontal, and 180° to the vertical field with polarity opposite that of the umbra. Positive v_r and v_z values (blue-to-black colors) indicate outflows and upflows, respectively. Note that this sign convention differs from the one used in observational studies, which normally follow the spectroscopic definition of flow velocities along the line of sight, where negative values denote flows moving toward the observer and positive values denote flows moving away from the observer. Black contour lines indicate the regions where the intensity $I < 0.45I_0$ and $I < 0.9I_0$. The images correspond to the same snapshot as Figure 1.

some regions within the penumbra at $\log(\tau) = -2.0$, -0.8 , and 0 where the radial velocity is negative, indicating photospheric inflows occur

along penumbral filaments. Their associated vertical velocity shows large negative values (downflows) close to the inner penumbral boundary, at the end of these inflow filaments.

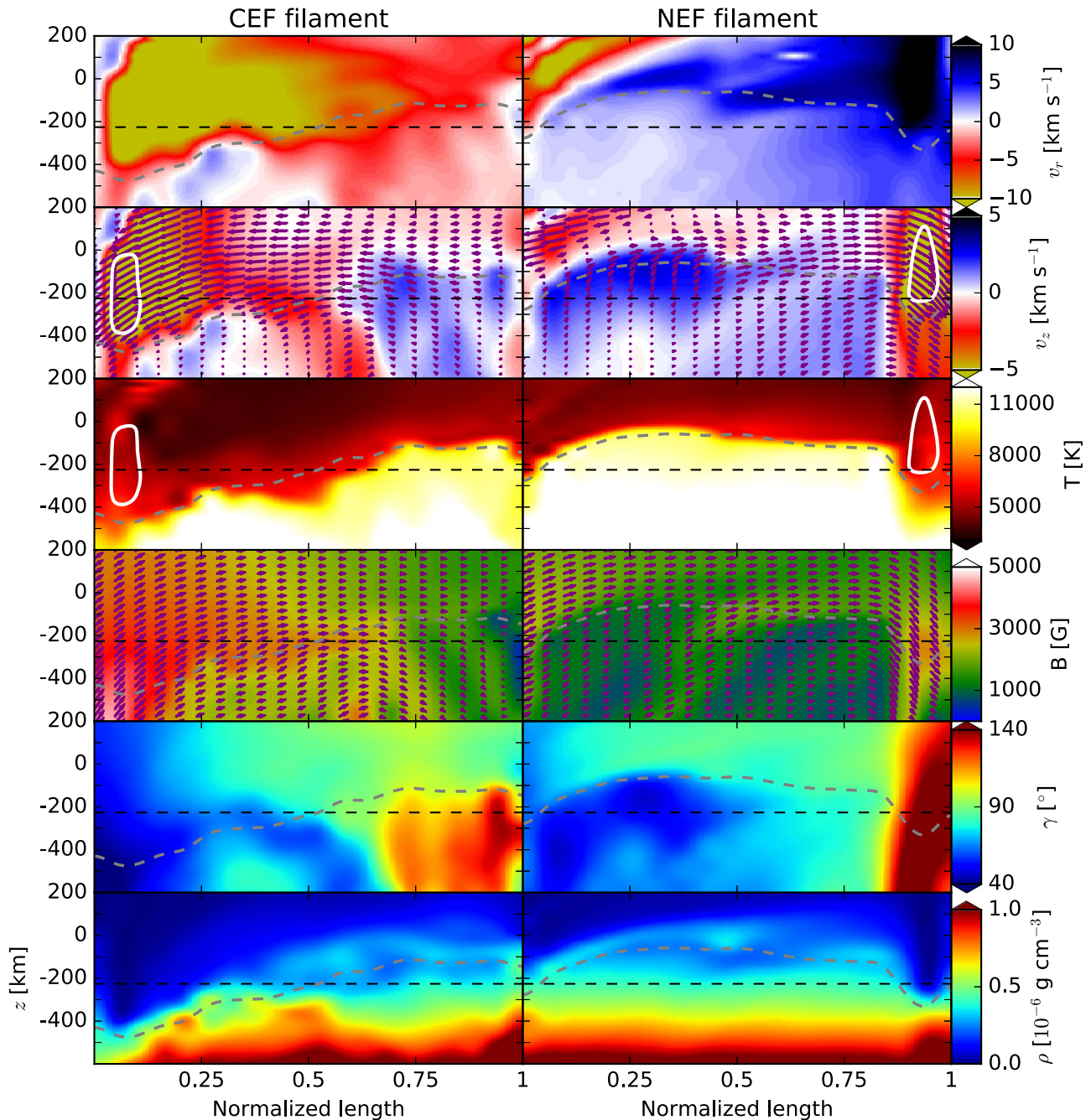


Figure 3. Vertical cross-section through the central axes of two filaments, reaching from -600 km to 200 km above the surface: (left) CEF-carrying filament and (right) NEF-carrying filament. The filaments were selected from the snapshot at $t \sim 67$ solar hours, which corresponds to a time when the CEF is prominent and stable. Panels show, from top to bottom: radial flow velocity v_r , vertical flow velocity v_z , temperature T , magnetic field intensity B , field inclination with respect to vertical γ , and density ρ . Gray dashed lines indicate the $\tau = 1$ levels. Horizontal dashed lines are placed at $z = -226$ km, which is the average height of $\tau = 1$ in the penumbra with respect to the quiet Sun. The arrows in the v_z and B maps indicate the direction of the flow and magnetic field, respectively, mainly to guide the eye. The white contour lines on the v_z and T maps indicate sink regions with supersonic downflows, i.e., where $v_z < -8$ km s $^{-1}$. As a reference, the sonic speed is about 6 km s $^{-1}$ close to the $\tau = 1$ surface. The orientation of the panels is such that the umbra is located to the left.

In order to gain insight regarding the physical differences between the regions harboring the counter-EF (CEF) and those with a normal EF (NEF), in Figure 3 we compare the characteristics of the gas and the magnetic field along the central axes of two radial flow channels that carry a CEF and an NEF, respectively. Figure 3 shows a vertical cross-section along the normalized central axes of the two selected penumbral filaments, a CEF-carrying filament (left panels) and an NEF-carrying filament (right panels), from $z = -600$ km to 200 km above the surface (which is defined

as the average height of the $\tau = 1$ level in the quiet Sun). The selected individual filaments are representative of each filament type (CEF-carrying and NEF-carrying, respectively) because most of the qualitative physical characteristics discussed below are true for most of the filaments in this snapshot.

The velocity panels in Figure 3 show the sources of the NEF, i.e., the portion of the filament on the right panels that harbors both upflows ($v_z > 0$) and outflows ($v_r > 0$), spanning around 85% of the filament's normalized length, while the sinks (regions where $v_z < 0$ and $v_r > 0$) are observed toward the

outermost 15% of the filament’s length. In contrast, the sources of the CEF (regions where $v_z > 0$ and $v_r < 0$ on the left panels) are located in the outer endpoint of the filament (i.e., in the endpoint closer to the quiet Sun) from ~ 0.6 to 1 in the normalized length scale, while their sinks (regions where $v_z < 0$ and $v_r < 0$) dominate mainly within the innermost 30% of the filament. Therefore, unlike the CEF-carrying filament, almost the entire NEF-carrying filament behaves as a source of flow.

Nonetheless, there are also some similarities. In both the CEF and NEF flow channels, the upflows harbor hot gas ($T > 10,000$ K) and are associated with relatively weak magnetic fields. The magnetic field in the upflow cells becomes more inclined with height and is aligned with the direction of the flows (see arrows on v_z and B panels in Figure 3). Furthermore, in both the NEF and CEF, the gas flows are supersonic in the sink regions and exhibit lower temperatures than at their sources ($T < 8000$ K). The downflowing gas at the sink regions is slightly warmer than in its surroundings, and the downflow speeds are generally supersonic at these locations, dropping rapidly with depth from supersonic to subsonic. These properties suggest that, for both the NEF and CEF, deceleration takes place in the form of shocks.

Compared to the field strength at the source regions ($B < 2000$ G) in both CEF and NEF, the magnetic field presents a strengthening at the sink regions ($B > 2500$ G), where it gradually becomes more vertical in the flow direction. Furthermore, in both NEF and CEF, the magnetic field polarity in the sink regions is opposite to that at their corresponding sources. In Figure 3, because we concentrate on the central axes of the filaments, we see only the “end of filament” sinks. Nonetheless, most of the overturning mass flux goes to the lateral sinks, so the end of filament sinks represent only a part of the picture because a significant fraction ($\sim 50\%$) of the returning mass flux is found in regions with a field that is still pointing upward when the lateral sinks are included.

Dashed gray lines in Figure 3 indicate the variation in height of the $\tau = 1$ levels along the two flow channels, with respect to the reference penumbral average height $z = -226$ km (horizontal black dashed lines). Such constant optical depth levels are depressed in the downflowing part of the filaments and are elevated in the upflowing part of the filaments. The depression of the constant optical depth surfaces in the sink regions is caused by the lower temperatures and densities of the downflowing gas compared to the upflowing gas. This is an important aspect to consider in observational studies of penumbral filaments, in which the dynamics of the flows and the magnetic field structure are only accessible at constant optical depth surfaces (see also the discussion in van Noort et al. 2013). In this simulation, the magnetic field strength suffers a large enhancement in the downflowing part of the filaments (sinks) along the $\tau = 1$ level, taking values of up to ~ 5 kG in the CEF filament and ~ 2.5 kG in the NEF-carrying filament. For the CEF filaments, such a tremendous strengthening of the field is partly the result of the strong depression of the $\tau = 1$ level at the sinks and their close vicinity to the umbral field (note that the CEF sinks are mainly located close to the umbral boundary). The strengthening of the field at the sinks of the CEF filaments at constant geometrical height also contributes (as can be seen in the left column of Figure 3). Moreover, the sinks of the NEF filaments also present a field intensification near the $\tau = 1$ level. Such local field

strengthening might be produced by the supersonic downdrafts of magnetized flux concentrations at the sink regions, as suggested by van Noort et al. (2013) to explain the observation of field strengths on the order of 7 kG in supersonic downflow regions at the outer penumbra of a sunspot.

3.2. Driving Forces of the Penumbral Flows

Our following analysis is similar to the analysis performed by Rempel (2011), which aimed to investigate the physical processes that lead to the driving of large-scale outflows around sunspots. Therefore, in order to investigate which forces are responsible for driving the inflows and the outflows in the penumbra, we analyze the various terms in the kinetic energy equation used by MURaM, which is derived from the momentum equation. Because we concentrate on time averages within this section, we use the following energy balance equation, which neglects the temporal derivatives and assumes stationary flows:

$$\underbrace{\mathbf{v} \cdot (\rho \mathbf{g} - \nabla p)}_{\text{Pressure}} + \underbrace{\mathbf{v} \cdot (\mathbf{j} \times \mathbf{B})}_{\text{Lorentz}} - \underbrace{\rho \mathbf{v} \cdot [(\mathbf{v} \cdot \nabla) \mathbf{v}]}_{\text{Acceleration}} + \underbrace{\mathbf{v} \cdot \mathbf{F}_{\text{visc}}}_{\text{Viscosity}} = 0. \quad (1)$$

In this energy balance equation, a negative acceleration term represents a source of kinetic energy—given that, under the assumption of stationarity, the acceleration term is identical to the negative divergence of the kinetic energy flux, $\rho v^2/2$.

We compute the individual terms in the energy balance equation as follows:

$$\langle P_i^\pm \rangle = \langle v_i^\pm [\rho g_i - (\nabla p)_i] \rangle \quad (2)$$

$$\langle L_i^\pm \rangle = \langle v_i^\pm (\mathbf{j} \times \mathbf{B})_i \rangle \quad (3)$$

$$\langle A_i^\pm \rangle = \langle -\rho v_i^\pm [(\mathbf{v} \cdot \nabla) \mathbf{v}]_i \rangle. \quad (4)$$

The viscosity term is not explicitly calculated; instead, we use an approximated magnitude that we call *residual force*:

$$\langle R_i^\pm \rangle = \langle -(P_i^\pm + L_i^\pm + A_i^\pm) \rangle. \quad (5)$$

In Equations (2)–(5), i indicates the Cartesian coordinates and the brackets indicate temporal averages over 10 hr, from $t = 60$ –70 hr after initialization of the simulation. We then use the transformation to cylindrical coordinates to separate the directions along and perpendicular to the penumbral filaments, r and z coordinates, respectively. Here, v_i^\pm denotes positive and negative velocity components, respectively (v_r^+ represents outflows and v_z^+ upflows).

The top panels of Figure 4 show the azimuthally and temporally averaged vertical slices of the radial velocity separately for all the inflows (left) and all the outflows (right) in the penumbra, i.e., using masks that select only the grid points where $v_r < 0$ and $v_r > 0$, respectively, from $z = 0.5$ to -3 Mm (relative to the average height of the $\tau = 1$ level in the quiet Sun). The NEF-related outflow speeds larger than 2 km s^{-1} , and in some places even larger than 5 km s^{-1} , stand out close to the $\tau = 1$ level, being generally restricted to below $\tau = 0.01$. Note that, in this case, the mask excludes any inflow occurring in the penumbra, even those corresponding to the IEF-like feature that dominates the penumbra above $\tau = 0.01$ (see radial velocity maps in Figure 2). In contrast, the inflow speeds above 2 km s^{-1} , which also stand out close to the $\tau = 1$ level due to the CEFs, produce a continuously increasing

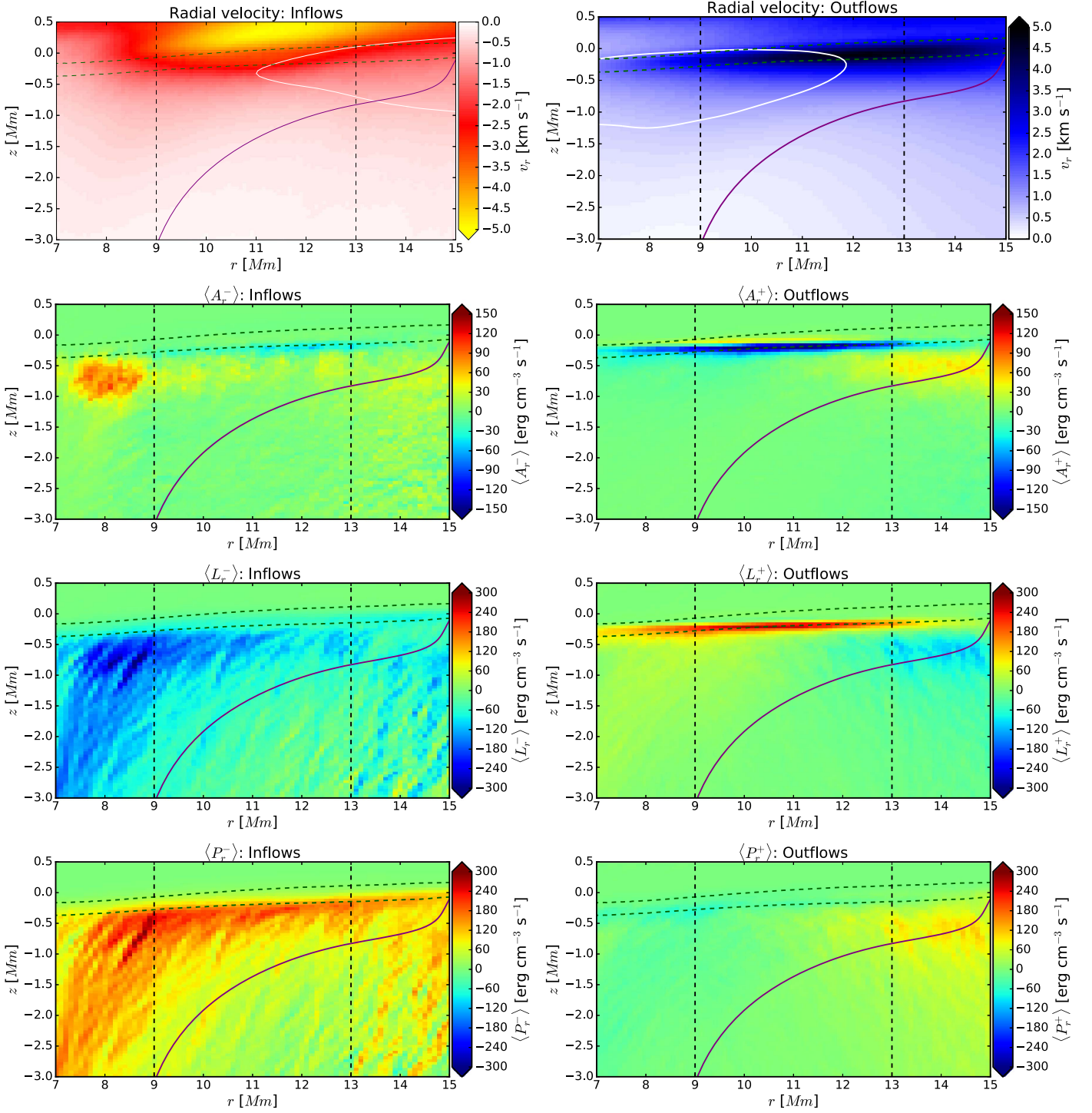


Figure 4. Radial flow velocity and radial energy conversion terms as functions of radius and height, using masks that respectively select only inflows ($v_r < 0$, left plots) and only outflows ($v_r > 0$, right plots) in the penumbra. All plots were averaged from 60 to 70 solar hours using the half spatial resolution 3D cubes at a temporal cadence of 900 sec. From top to bottom: radial flow velocity, and radial components of the acceleration, Lorentz, and pressure forces. The residual terms in both cases are negligible. Vertical dashed lines delimit the inner ($r = 7\text{--}9$ Mm from the center of the sunspot), middle ($r = 9\text{--}13$ Mm), and outer penumbrae ($r = 13\text{--}15$ Mm), as indicated by the cyan circles in Figure 1. Green dashed lines indicate the averaged $\tau = 1$ and $\tau = 0.01$ levels. The purple curve is an azimuthally and temporally averaged iso-contour placed at $B = 950$ G and used as a reference to distinguish between the high- and low-field regions in the penumbra. White contour lines on the top plots enclose regions with vertical upflow speeds larger than 0.3 km s^{-1} when using masks that select only the sources of inflows (i.e., grid points where $v_r < 0$ and $v_z > 0$, left) and the sources of outflows (i.e., grid points where $v_r > 0$ and $v_z > 0$, right).

inflow profile toward the higher layers due to the inclusion of all those inflows in the IEF-like feature that peaks above $\tau = 0.01$. It is not in the scope of the present work to analyze such an IEF-like feature. Moreover, given that these inflows occur close to the top boundary of the simulation box, which is

numerically closed, they likely are highly influenced by the upper boundary conditions.

Figure 4 also shows the resultant radial energy conversion terms in the penumbra, separated for all inflows ($\langle A_r^- \rangle$, $\langle L_r^- \rangle$ and $\langle P_r^- \rangle$, plots on the left) and for all outflows ($\langle A_r^+ \rangle$, $\langle L_r^+ \rangle$ and

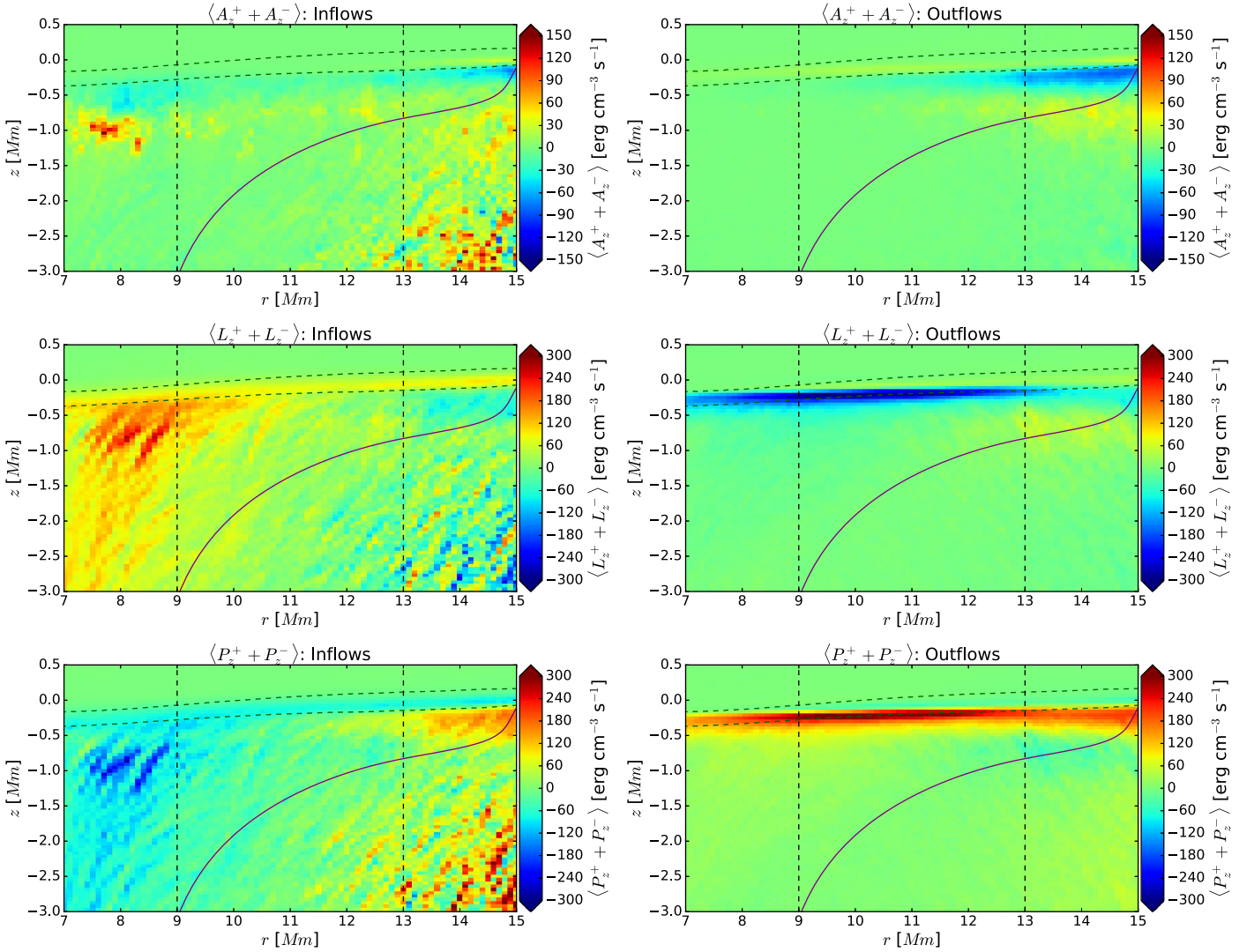


Figure 5. Vertical energy conversion terms as functions of radius and height in the penumbra (azimuthal and temporal averages). From top to bottom: $\langle A_z^+ + A_z^- \rangle$, $\langle L_z^+ + L_z^- \rangle$, and $\langle P_z^+ + P_z^- \rangle$ in inflow regions (panels on the left) and in outflow regions (panels on the right). Same format as plots in Figure 4.

$\langle P_r^+ \rangle$, plots on the right). Recall that these energy conversion profiles show the 10 hr average of the azimuthally averaged terms in each mask. Negative values of A_r^- and A_r^+ indicate inward and outward acceleration of the fluid, respectively. Likewise, positive values of P_r^- and L_r^- represent a source of kinetic energy for inflows, while positive values of P_r^+ and L_r^+ represent an energy source for outflows.

Panels in Figure 5 are in the same format as those in Figure 4 and show the vertical energy conversion terms ($\langle A_z^+ + A_z^- \rangle$, $\langle L_z^+ + L_z^- \rangle$ and $\langle P_z^+ + P_z^- \rangle$) associated with the inflows (panels on the left) and outflows (panels on the right). There, negative values of $A_z^+ + A_z^-$ indicate vertical acceleration of the fluid in inflow and outflow regions, accordingly.

While most of the radial acceleration of the fluid takes place within the inner and middle penumbra for the outflows (negative values of $\langle A_r^+ \rangle$ in Figure 4), the inflows are predominantly accelerated within the middle and outer penumbra (negative values of $\langle A_r^- \rangle$).

These regions are confined to a narrow layer near the $\tau = 1$ level. There, the Lorentz force is the primary driver of the outflows, while the pressure terms have a weakly negative

energetic contribution. In contrast, the inflows are driven mainly by the radial pressure forces, while the radial Lorentz force shows a negative contribution on average. However, plots in Figure 6 reveal that the radial Lorentz term contributes mostly positively close to $\tau = 1$ when the masks only include the regions responsible for driving inflows (i.e., source regions where both $v_r < 0$ and $v_z > 0$), and neglect those regions where the inflows sink (i.e., regions where $v_r < 0$ and $v_z \leq 0$).

Plots in Figure 4 also show that, in deeper layers, the radial pressure terms are almost in balance with the radial Lorentz terms, resulting in only minor acceleration of outflows and inflows in the deep penumbra. Likewise, almost no driving forces exist above $\tau = 0.01$. Toward the inner penumbra for the inflows and outer penumbra for the outflows, the layers below the $\tau = 1$ level display a similar forcing pattern, though the energy conversion is on average larger at the inner penumbra for inflows than at the outer penumbra for outflows. In both cases, from $\tau = 1$ down to $z \sim -1$ Mm, the radial Lorentz force overcompensates the radial pressure driving, producing a radial deceleration of inflows and outflows (positive values of $\langle A_r^- \rangle$ and $\langle A_r^+ \rangle$, respectively). However, this energy is transferred into a vertical acceleration of the fluid

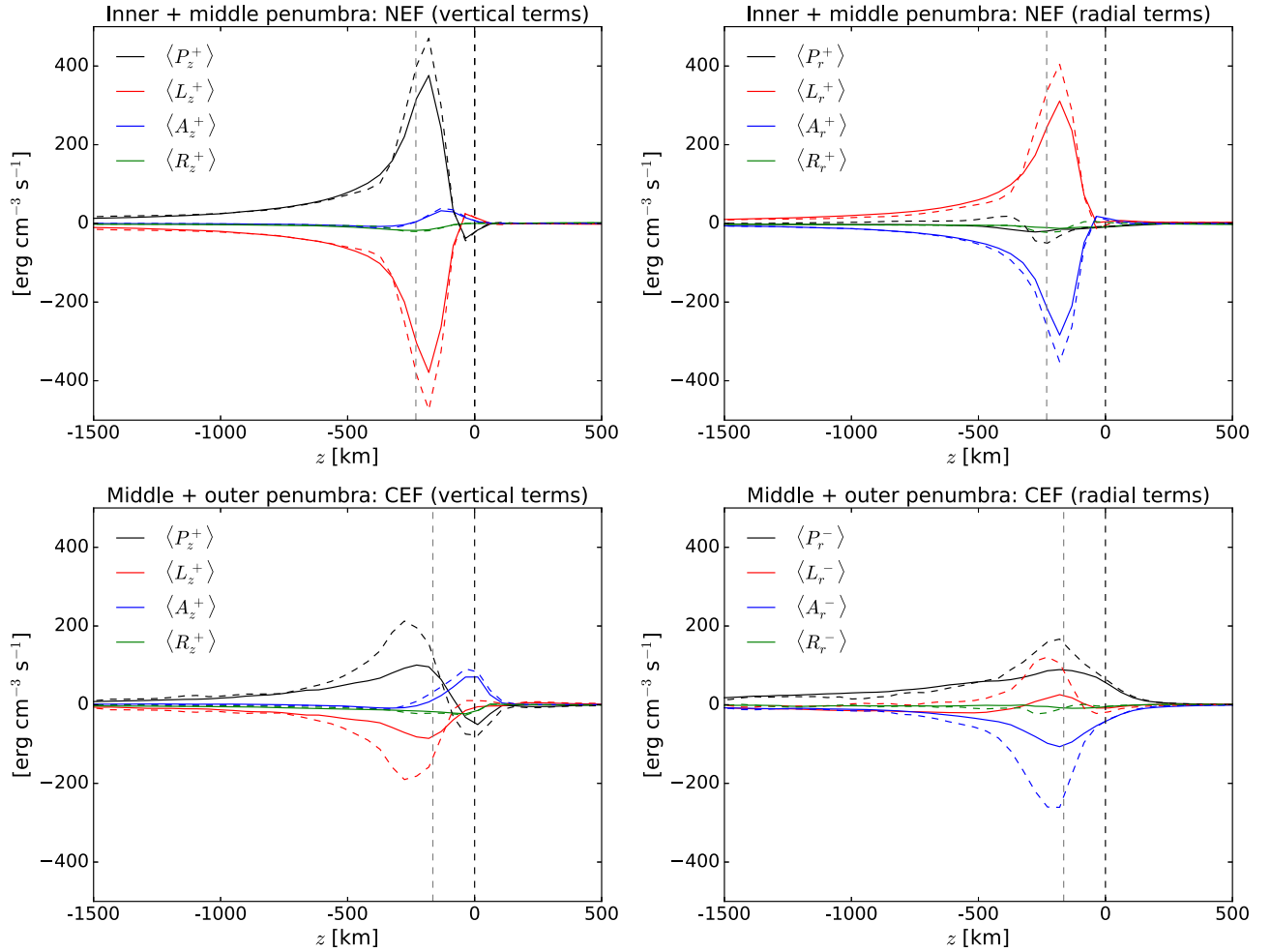


Figure 6. Height dependence of the energy conversion terms in the kinetic energy equation. The solid curves show the energy terms averaged in time (from 60 to 70 hr) and at each height for the regions that have both upflows and outflows ($v_z > 0$ and $v_r > 0$, upper plots) and for those with both upflows and inflows ($v_z > 0$ and $v_r < 0$, lower plots). The dashed curves show the averaged energy terms when using a mask that extracts the penumbral filaments carrying the CEF and the NEF, correspondingly, and neglects the contribution of all other flows (e.g., those occurring beyond the reference iso-contour at $B = 950$ G shown in Figures 4 and 5). We considered only flows in the inner and middle penumbra for the plots on the top, and in the middle and outer penumbra for the plots on the bottom. The energy conversion terms are separated into their vertical (left plots) and radial components (right plots). Black: pressure forces, red: Lorentz forces, blue: acceleration forces, green: residual forces. The vertical dashed lines are placed at $z = 0$ km (black) and at the average height of the $\tau = 1$ level in the corresponding regime(s) of the penumbra, which are indicated in the headers of each plot.

(negative values of $\langle A_z^+ + A_z^- \rangle$ in Figure 5). Such vertical acceleration is mainly downward at the inner penumbra for inflows and at the outer penumbra for outflows, i.e., negative values of A_z^- dominate in the $\langle A_z^+ + A_z^- \rangle$ average profiles at those places. Finally, the downflowing gas is decelerated again close to $z = -1$ Mm. This is seen as the change into positive values of $\langle A_z^+ + A_z^- \rangle$ in Figure 5. In the case of the outflows, a transition toward “normal” overturning convection (i.e., more granular-like upflows and downflows where vertical pressure forces lead mostly to vertical acceleration) starts taking place in the region $r > 13$ Mm. This also contributes to the strong positive $\langle A_z^+ + A_z^- \rangle$ found right below $\tau = 1$, which also coincides with positive $\langle P_z^+ + P_z^- \rangle$.

As mentioned above, most of the radial acceleration occurs from the middle-to-outer penumbra in inflows, and from the inner-to-middle penumbra in outflows. Such penumbral regimes also correspond to the average location of the respective flow source regions (see white contour lines in Figure 4). Therefore, plots in Figure 6 (solid curves) have been created by using a mask that specifically selects the sources of the outflows (regions where $v_z > 0$ and $v_r > 0$) within the inner

and middle penumbra at each height, and the sources of the inflows (regions where $v_z > 0$ and $v_r < 0$) within the middle and outer penumbra at each height. The average depth profile of the energy conversion terms at the sources of each flow are then averaged in time (10 hr). Plots in Figure 6 show that most of the energy conversion takes place between $z = -500$ and 0 km, and represents the driving of the NEF and the CEF, correspondingly.

However, the solid curves in Figure 6 stand for the sources of everything that is flowing outward (upper plots) and the sources of everything that is flowing inward (lower plots) in the respective penumbral regimes. This includes the filaments of interest carrying the NEF and the CEF, respectively, but there are also other, smaller-scale flows that do enter the average. The weight or contribution of such flows to the average energy conversion terms seems to be negligible below $z \sim -500$ km (by comparing with the dashed curves in Figure 6), but is larger in the near-surface layers (between $z = -500$ km and $z = 0$) where the driving of the NEF and the CEF occurs. However, those additional flows do not modify the average energy balance of the NEF. Only in the radial energy balance of the

CEF do we see an increased contribution of the radial Lorentz term to the inward acceleration of the fluid when neglecting other inflows. This is because those additional inflows are mainly driven by radial pressure forces in regions where L_r^- is generally null or slightly negative.

In both NEF and CEF sources, the upflow components show an approximate balance between P_z^+ and L_z^+ , mainly below and close to $\tau = 1$. Higher up, the vertical pressure driving, which includes the contribution of gravity, changes sign; the A_z^+ becomes positive just below $z = 0$, implying upflows that decelerate before reaching the photosphere. The steepening of P_z^+ in the near-surface layers is caused by the presence of strong magnetic fields. However, the field strength is a factor of $\sim 2-3$ weaker in the outer penumbra than in the inner penumbra, which explains why the energy conversion is lower at the sources of the CEF than at the sources of the NEF, and might be related to the transient and unstable aspects of the CEFs.

For the NEF, we find that the energy extracted by the Lorentz force in the vertical direction, L_z^+ , is almost completely transferred to the radial outward acceleration of the fluid, A_r^+ , similar to the findings of Rempel (2011). The energy conversion by radial Lorentz force, L_r^+ , is mainly balanced by A_r^+ , and P_r^+ has a slightly negative contribution close to $\tau = 1$. This can be thought as a deflection of the vertical pressure driving by the Lorentz force ($v_z B_r \approx v_r B_z$), i.e., the magnetic field forms an almost 90° nozzle connecting the pressure driving in the vertical direction to a radial outward acceleration. The Lorentz force does not do any net work. The ultimate energy source is the pressure force due to a large vertical pressure gradient that steepens in the near-surface layers.

In normal convection, a loss of buoyancy of the gas near $\tau = 1$ causes a deceleration of the upflows, and the gas is pushed horizontally to all sides by the rising gas underneath it (i.e., the decelerating gas builds up excess pressure which drives horizontal flows) because it cannot go any higher. In the NEF, there is also a loss of buoyancy of the gas near $\tau = 1$, but in this case the horizontal pressure gradients only play a role in the azimuthal direction (i.e., to drive the horizontal lateral flows) and have slightly negative contribution in the radial direction. For the NEF, it is the inclined magnetic field in the penumbra that plays the most important role. Because there is a magnetic field that points mainly in one direction in the penumbra, the gas motion loses degrees of freedom and therefore moves in a preferred direction (the radial one). However, the field is not the main accelerating agent of the gas flow in the radial direction, i.e., the density of the gas decreases at the surface where it is deflected radially, and its speed must be higher because of mass flux conservation. The gas accelerates outward because more and more gas is coming from below, all along the filament; i.e., mass conservation requires the gas to move faster and faster horizontally. While in granulation, the horizontally flowing gas can isotropically carry away mass on the horizontal plane, there are less degrees of freedom in the penumbra, due to the magnetic structure. Therefore, the horizontal flows must be faster in penumbra than in granules to carry away the same amount of mass (assuming equally strong upflows and equal horizontal size of upflowing patches). However, the existence of downflows at the sides of the filaments also removes part of the horizontally flowing mass, therefore limiting the speed of the radial flows.

In contrast, the CEF is predominantly driven by radial pressure forces (and so are all inflows at all heights). There is an additional positive contribution from the radial Lorentz force close to $\tau = 1$, and the combination of both (magnetic and pressure forces) leads to the inward acceleration of the fluid. The role of the radial Lorentz term in driving inflows in the near-surface layers becomes more important when we extract only the CEF-carrying filaments (dashed lines in Figure 6).

Similarly to the situation at the sources of the NEF, the upflowing gas at the sources of the CEF experiences a transition from a more vertical to a more horizontal field, due to a bending of the field occurring at the outer and middle penumbra (see, e.g., the field inclination along the CEF filament shown in Figure 3). Thus, at the sources of the CEF, the upflowing gas is partly deflected inward by the magnetic field (note that part of the energy extracted by the magnetic field in the vertical direction is transferred into the inward acceleration of the gas). However, unlike the outflows, the inflows are primarily driven by radial pressure forces, making the CEF a strong candidate for a siphon flow, which is further supported by our analysis in Section 4.

3.3. Temporal Evolution of the CEF

Figure 7 follows the evolution in time of a portion of the penumbra with CEF. We focus only on a single CEF patch because—although the time evolution of the CEF patches in different parts of the penumbra are rather independent of each other—the general results described below are true for all the simulated CEF patches.

In panel (a), the figure shows the radial mass fluxes at three stages of the evolution of the CEF in the selected penumbral sector at $z = -226$ km; the negative values indicate mass flowing radially inwards. Panels (b), (c), and (d) in Figure 7 show that the source regions of the CEF at $z = -226$ km that have positive values of L_r^- are all characterized by negative values of B_z , i.e., downward-pointing fields ($\gamma > 90^\circ$), regardless of whether they are located in the middle or outer penumbra. In those regions, the field inclination increases radially inward. Panel (e) shows the radial energy conversion associated with the sources of the CEF in the different time steps. The contributions of both L_r^- and P_r^- to the inward acceleration of the fluid vary over time, being the increase of the overall radial energy conversion associated with an increase of the radial mass flux in the selected CEF patch. At all three stages of the CEF shown in Figure 7, the vertical pressure force shown in panel (f) presents a steepening close to $z = -500$ km; it peaks near the average $\tau = 1$ level of the penumbra ($z = -226$ km), keeping a close balance with work done against the Lorentz force.

In order to gain insight into the typical underlying magnetic structure of the regions responsible for driving the CEF, in Figure 8 (left panel) we show the average vertical and radial magnetic field as a function of height in regions that are sources of CEF (red) and those that are sources of NEF (blue). For the CEF sources, the vertical field component (dashed red line) remains constant at about 400 G below $z = -226$ km and decreases to ~ 100 G in higher layers. The radial field component (solid red line) increases monotonically from about 700 G to ~ 1000 G below $z = -226$ km. At $z \sim -226$ km, the slope of $|B_r|$ suffers a large steepening and the radial field component increases to almost 1400 G toward $z = 0$ and remains nearly constant at higher layers. The steep increase of

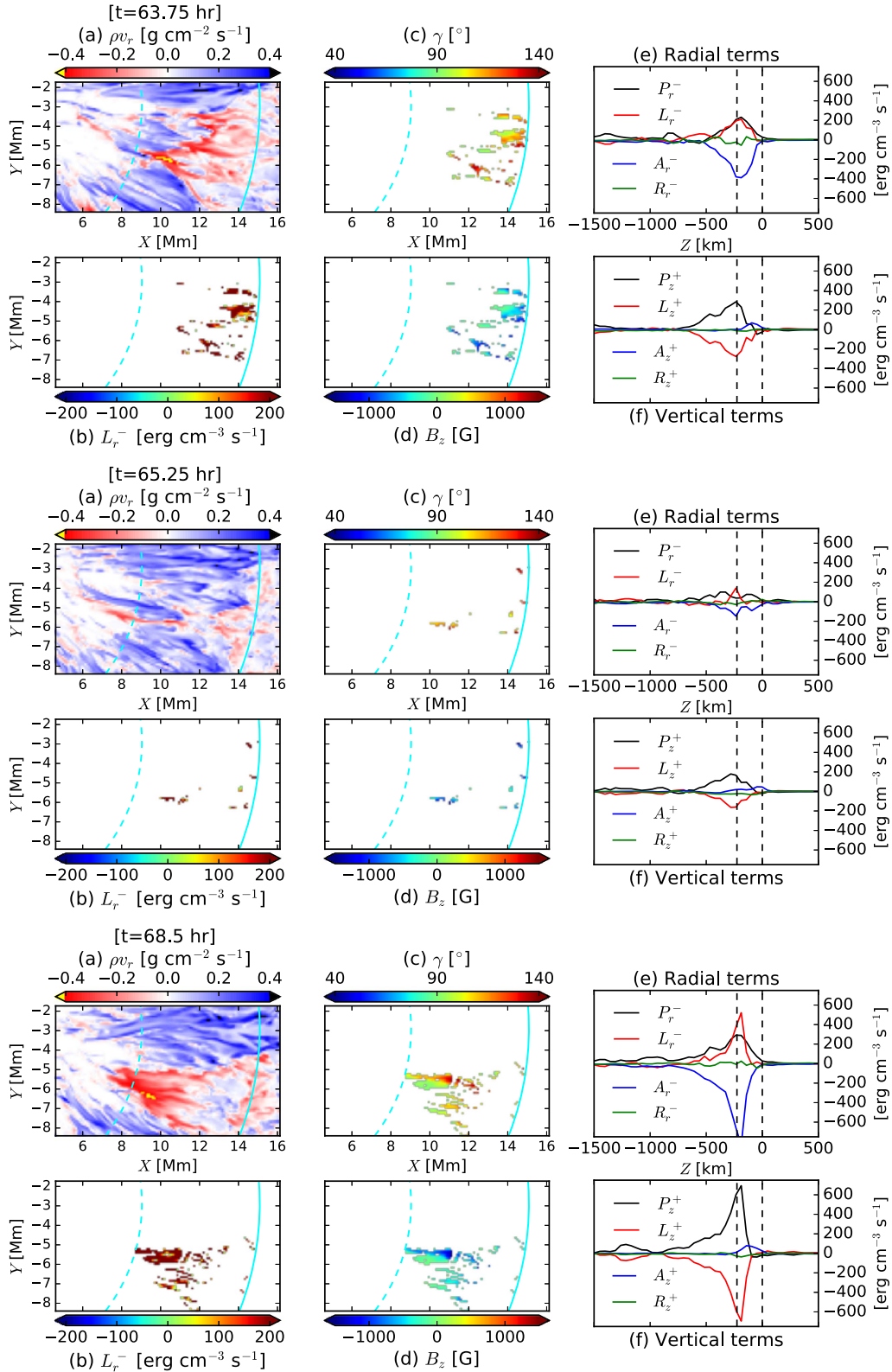


Figure 7. Variability of the CEF in a portion of the penumbra at three selected time steps, from top to bottom: $t = 63.75$, 65.25 , and 68.5 hr. For each time step, six panels are plotted. Panel (a) displays the radial mass flux, ρv_r , at $z = -226$ km. Panels (b), (c), and (d) show the quantities L_r^- , field inclination γ , and vertical field component B_z , respectively, in the regions responsible for driving the CEF at $z = -226$ km, where the term L_r^- has positive values. In panels (a)–(d), cyan curves were placed at $r = 9$ Mm (dashed) and $r = 15$ Mm. Panels (e) and (f) depict the height profiles of the radial and vertical energy conversion terms, respectively. The energy conversion terms have been averaged over the sources of the CEF at each height and time step, using the same mask as in the dashed plots of Figure 6. The vertical dashed lines in panels (e) and (f) are placed at $z = 0$ km (average height of the $\tau = 1$ level in the quiet Sun) and $z = -226$ km (average height of the $\tau = 1$ level in the penumbra).

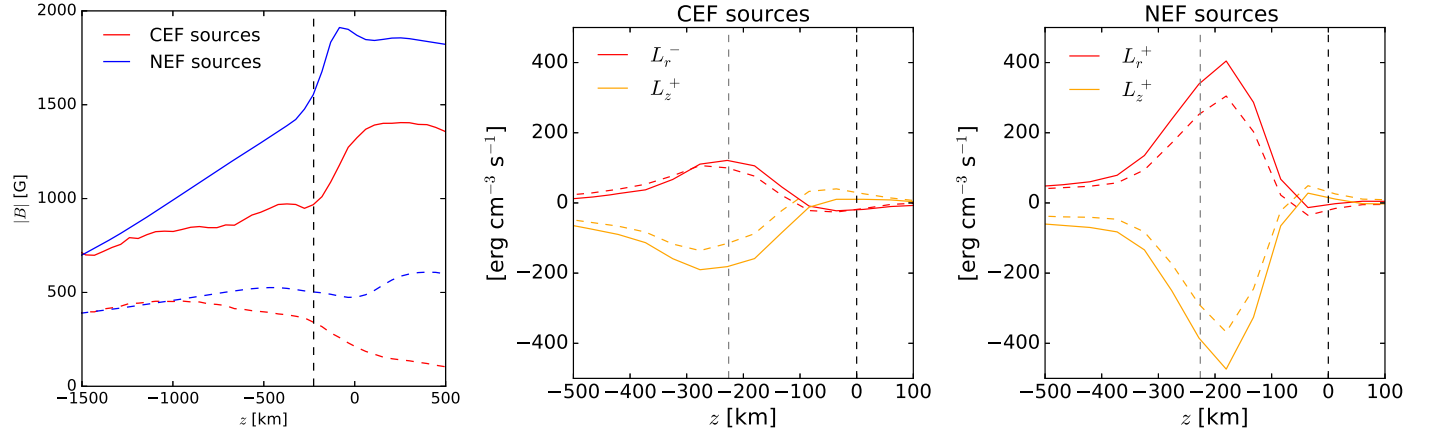


Figure 8. Left panel: temporal average of the magnetic field vertical profiles in regions responsible for driving the CEF (red) and NEF (blue). The magnetic field is separated according to its vertical (dashed) and radial (solid) components. The vertical dashed line is placed at $z = -226$ km. Middle panel: energy conversion by radial (red) and vertical (orange) Lorentz force at the sources of the CEF. Solid lines are a close-up view from the corresponding dashed lines in Figure 6. The dashed lines show the simplified expression: $L_r = v_r \frac{1}{4\pi} B_z \frac{\partial B_r}{\partial z}$ (red) and $L_z = -v_z \frac{1}{4\pi} B_r \frac{\partial B_r}{\partial z}$ (orange). Right panel: same as in the middle panel for the sources of the NEF.

$|B_r|$ near $\tau = 1$ combined with the reduction of $|B_z|$ results in a strong increase of the radial Lorentz force. As shown in the middle panel of Figure 8, there is a good agreement between the Lorentz terms as defined in Equation (3) (solid lines) and the following approximations:

$$L_z \approx -v_z \frac{1}{4\pi} B_r \frac{\partial B_r}{\partial z} \quad (6)$$

$$L_r \approx v_r \frac{1}{4\pi} B_z \frac{\partial B_r}{\partial z}, \quad (7)$$

which are indicated by the dashed lines. Similar to what happens at the NEF sources (right panel), the energy extracted at the CEF sources in the vertical direction by the Lorentz force, L_z , is in approximate balance with the radial Lorentz force, L_r . Hence, for both NEF and CEF sources, the following is valid:

$$v_z \frac{1}{4\pi} B_r \frac{\partial B_r}{\partial z} \approx v_r \frac{1}{4\pi} B_z \frac{\partial B_r}{\partial z}, \quad (8)$$

which leads to the relation $v_z B_r \approx v_r B_z$. This relation implies a deflection of the vertical pressure forces in upflows by the Lorentz force in order to allow for the strong acceleration in the radial direction; this is in agreement with the findings of Rempel (2011) for the driving mechanism of the NEF. Here, we show that this relation is also valid for the CEF, whose vertical flows occur in regions where the vertical field component is negative and its magnitude decreases with height, while the upflowing gas encounters an increased radial field component when it reaches the surface. This results in a radial driving by the Lorentz force that favors inflows and accelerates the gas inward with the help of radial pressure forces, which are larger than the Lorentz force in this case.

Similarly, at the source regions of the NEF, the average vertical field component (dashed blue line in left panel of Figure 8) remains around ~ 400 G while the radial field component (solid blue line) increases steadily from ~ 700 G to ~ 1500 G just below $z = -226$ km. Just as at the CEF sources, the slope of $|B_r|$ suffers a strong steepening close to $z \sim -226$ km, such that $|B_r|$ increases up to 1900 G toward $z = 0$ and drops again in higher layers to about 1800 G. Note

that the average increase of $|B_r|$ near $\tau = 1$ is substantially larger for the NEF sources than for the CEF sources because they occur within different parts of the penumbra. This causes the contribution of the radial Lorentz term to be larger at the sources of the NEF than at those of the CEF.

Unlike the NEF, the CEF is driven at all times by the contribution of two different radial forces: P_r^- and L_r^- . Figure 9 shows the temporal evolution of the average radial mass flux in the near-surface layers (from $z = -500$ to 0 km) at the sources of the CEF in the selected penumbral portion (left plots), and for comparison, at the sources of the NEF (right plots). The plotted time interval covers the lifetime of the CEF (i.e., the time from 60 to 70 hr). The solid lines in Figure 9 show the average radial energy conversion terms in the near-surface layers at each time step. The temporal evolution of the CEF shows that the negative radial mass flux (dashed line) is strongly variable compared to the NEF case, and that it is proportional to the radial acceleration, A_r^- . This means that the sum of the two radial forces, magnetic and pressure (note that $A_r^- \approx -(L_r^- + P_r^-)$), is responsible for modulating the inward mass flux of the CEF in the near surface layers.

Unlike the CEF, the positive radial mass flux of the NEF and the radial energy balance have a more steady behavior during the 10 hr of the analyzed interval, exhibiting the quasi-stationarity and robustness of the NEF feature when the penumbra is well-developed. The radial Lorentz terms keep in balance with the radial acceleration forces during the 10 hr analyzed here, and they are consistently the forces responsible for driving the NEF in the radial direction.

4. Field-line Connectivity

We have shown in the previous analysis that the CEF and NEF are both driven within a thin boundary layer close to the $\tau = 1$ level, and that the velocity vector is mostly radial. Moreover, we found that strong radial pressure gradients exist everywhere within the thin boundary layer in which the CEFs are driven. In contrast, while the radial pressure forces have, on average, an opposed contribution to the driving of the NEF in the source regions, positive radial pressure forces dominate the average in the outer penumbra where the NEF sinks (Figure 4). Although the driving of the flows depends principally on the conditions in their respective upflow cells, identifying the

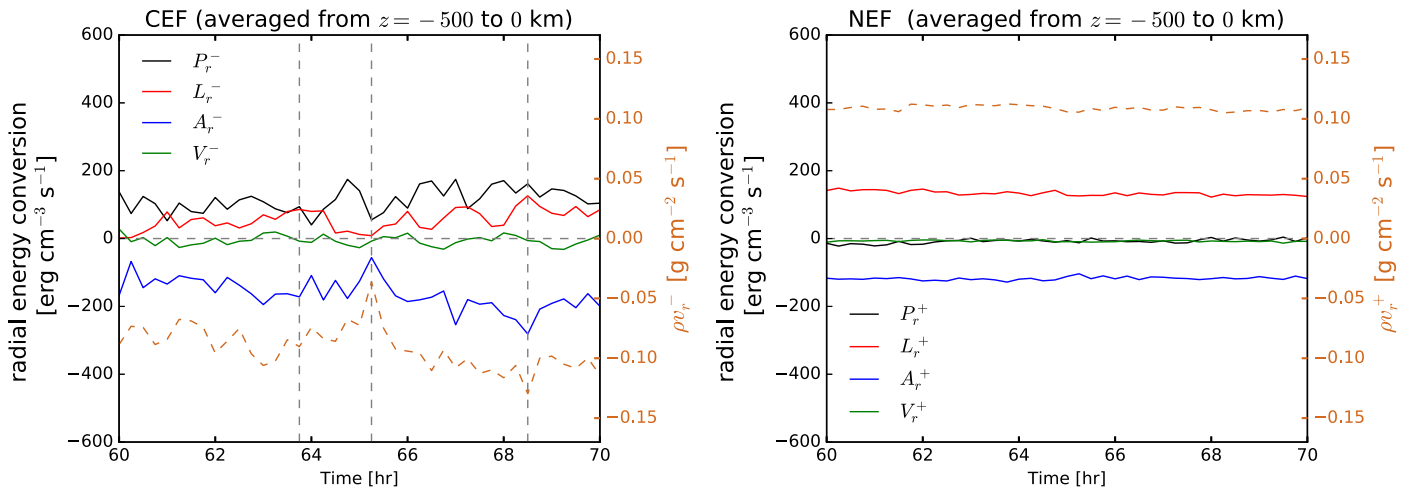


Figure 9. Temporal evolution of the radial forces (solid) and mass fluxes (dashed) at the sources of the CEF within the portion of penumbra shown in Figure 7 (left plots). At each time, the plots show the average value of each quantity in the near-surface layers (between $z = -500$ and $z = 0$ km) from the middle-to-outer penumbra. For comparison, we show the same average quantities for the sources of the NEF (right plots) averaged over the inner-to-middle penumbra. Vertical dashed lines on the left panel indicate the three selected stages of the CEF that are shown in Figure 7.

magnetic connectivity of the field lines is important to describing individual flow channels (penumbral filaments) as flux tubes, and therefore is also necessary to validate whether or not the flows are driven by a siphon flow mechanism. Nonetheless, such a representation involves some limitations when compared to models based on the thin flux tube approximation (e.g., Meyer & Schmidt 1968; Thomas & Montesinos 1993; Montesinos & Thomas 1997; Schlichenmaier et al. 1998a), which assume well-defined footpoints of the flux tubes on horizontal cuts made at given heights below the surface. In particular, the NEF-carrying filaments in this simulation (and in that by Rempel 2011) display elongated upflow cells that constrain their representation under the thin flux tube picture.

To study the magnetic field-line connectivity, as well as the associated field-aligned velocity component and pressure perturbation along the different types of filaments in the penumbra (NEF-carrying and CEF-carrying filaments), we use the VAPOR software package developed at NCAR (Clyne & Rast 2005; Clyne et al. 2007, <http://www.vapor.ucar.edu>).

In Figure 10, we have selected field lines in a cross-section perpendicular to filaments based on regions with strong horizontal flows. The selected field lines were colored according to their field-aligned velocity in the upper images and to the gas pressure perturbation along the field lines in the bottom images (we compute the pressure perturbation after subtracting the hydrostatic mean, because stratification dominates). The images on the left show field lines carrying a CEF from two different view angles and the images on the right show field lines carrying a NEF. In the case of the CEF filaments, most of the field lines span from the outer to the inner penumbra with a consistent inflow along them (top left panel) and they have a very systematic pressure perturbation (bottom left panel) with the gas flowing from high-pressure (purple) to low-pressure (white) regions, consistent with a siphon flow.

In the case of the NEF, the velocity along the field lines is less consistent—some field lines have even an inverse flow in their upper portion (top right panel), similarly to the findings of Rempel (2011). In particular, in the inner penumbra, field lines that host the fastest Evershed flows still connect to the top boundary, but small dips form between their extremes. This

indicates that the NEF is, to a lesser degree, a flow along the field; it also implies continuous reconnection and change of field line connectivity as the mass moves outward in the penumbra. Moreover, it implies that the physical conditions in the outer footpoint have a minor impact on the driving of the NEF. Looking at the pressure perturbation (bottom right), we find a mix of high and low pressure at both footpoints. There could still be siphon flows along some field lines (mostly in the outer penumbra), but they do not provide a consistent explanation for the Evershed flow in the bulk of the penumbra.

5. Discussion and Conclusion

We presented a detailed analysis of the properties of penumbral fine structure associated with the counter-Evershed flows (CEF) and the normal Evershed outflows (NEF) near $\tau = 1$ in the penumbra of the recent numerical sunspot simulation by Rempel (2015). Our investigation mainly focuses on the physical driving mechanisms of the NEF and CEF in the near-surface layers of this simulation.

The main difference found between the penumbral filaments carrying the NEF and those carrying the CEF is the location within the penumbra and the radial extent of the upflow cells. Both aspects are crucial for the driving of each type of flow, given that their driving mechanisms depend primarily on the conditions present in their respective upflow cells.

The energy conversion analysis at the sources of both outflows and inflows suggests that the CEF and the NEF are both driven within a thin boundary layer close to the $\tau = 1$ level, and no substantial driving forces exist well above $\tau = 1$. In both cases, the loss of buoyancy due to radiative cooling is seen as a change of sign of the work by pressure in the vertical direction close to $z = 0$ (Figure 6). However, while this provides only a small contribution to the deceleration of the vertical flow in the case of the NEF—i.e., most of the deceleration happens deeper, where the pressure driving is still positive and the dominant offset is given by the vertical Lorentz force—the deceleration of upflows by loss of buoyancy seems to be more prominent for the CEF near $z = 0$. Nonetheless, deceleration of upflows in CEFs near $\tau = 1$ occurs mainly due to an opposed contribution from the vertical Lorentz force, similarly to the NEF case. Therefore, notable differences exist

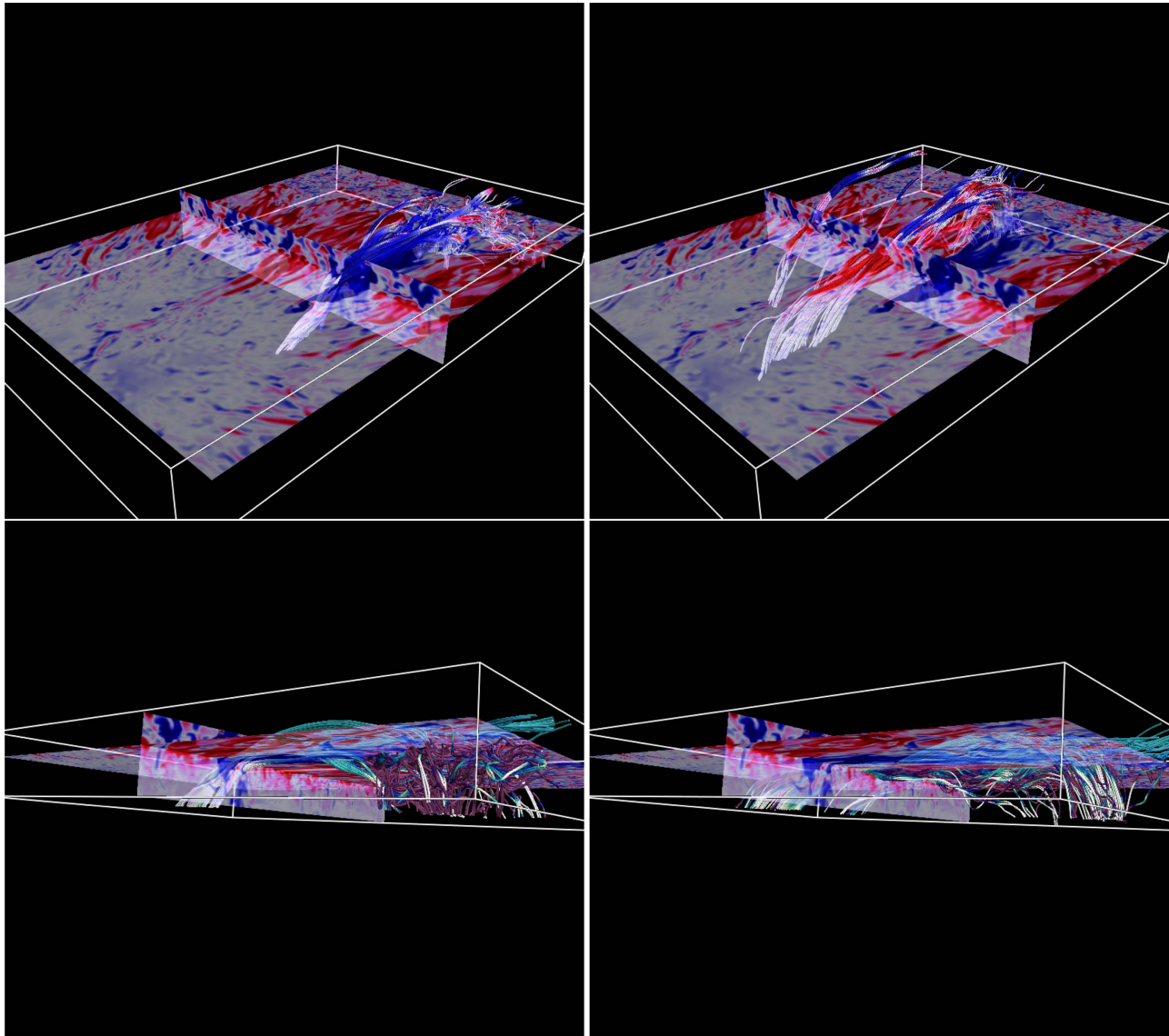


Figure 10. Field-line connectivity and associated velocity and pressure perturbations in the simulated penumbra: CEF filaments (left figures) and NEF filaments (right figures). In all figures, the semi-transparent horizontal and vertical planes show the field-aligned velocity component from $\pm 10 \text{ km s}^{-1}$ near the average $\tau = 1$ level; outflows are red and inflows are blue. The vertical plane is placed close to the inner penumbral boundary and used to select field lines by their flow velocity. In the upper figures, the color of the field lines shows the flow velocity along the field. In the bottom figures, the color of the field lines indicates the pressure perturbation along the field lines from $\pm 10^5 \text{ dyne cm}^{-2}$, where white is low and purple is high pressure. The upper and lower panels refer to different view angles. The plots correspond to the snapshot at $t = 65 \text{ hr}$.

with respect to the underlying driving forces of both NEF and CEF, compared to field-free convection where deceleration of vertical flows near the surface is mainly due to loss of buoyancy caused by the radiative cooling (see Rempel 2011, who analyzed in detail the driving of the NEF in a simulated sunspot penumbra, and made a comparison between the NEF and the plage region surrounding the sunspot; they found that the vertical pressure/buoyancy breaking has very clear distinct signatures in granulation and in the penumbra).

For the driving of the NEF, we found results similar to those reported by Rempel (2011). There is an almost complete balance between vertical pressure and Lorentz forces in upflows, as well as between the Lorentz force and acceleration in the radial direction. We found no significant kinetic energy in the vertical flow component at the sources of the NEF, but a strong acceleration in the radial component in the near-surface layers. This implies that the flow changes direction and

concurrently gains significant amounts of kinetic energy in the radial direction. Because the Lorentz force does not do any net work—it only changes the direction of the flow—we can say that the flow is deflected by the highly inclined magnetic field in the penumbra and the gas is accelerated in the radial direction as a result of mass flux conservation coupled with the low gas density at the surface. The most important feature driving outflows in the inner and middle penumbra is the increase of the radial field component close to $\tau = 1$. These results strongly support the magneto-convective driver scenario of the NEF, as proposed in Scharmer et al. (2008), where the NEF is described as the horizontal component of overturning convection in penumbrae.

It has also been proposed in some models that the NEF could be the result of stationary siphon flows driven by a gas pressure difference between the footpoints of the penumbral filaments (e.g., Meyer & Schmidt 1968). Such models consider processes

related to turbulent pumping near the outer penumbral boundary (Montesinos & Thomas 1997; Brummell et al. 2008), which make the field lines bend downwards and additionally produce a field strength enhancement in the outer filament endpoint due to strong downdrafts (van Noort et al. 2013). Such a field enhancement would establish a gas pressure gradient between the filament endpoints, producing a siphon-like outflow along the field lines. We do observe a net field strengthening at the outer endpoints of the NEF-carrying filaments (see, e.g., Figure 3) at the places where the NEF sinks in the outer penumbra. This enhanced field could explain the increase of the radial pressure gradient toward the outer penumbra, as seen in the bottom right plot in Figure 4. However, the radial pressure gradients do not play an important role in the inner or middle penumbra, where most of the driving of the NEF occurs. This can be attributed to the elongated aspect of the upflow cells, which produces a substantial reduction of the radial pressure gradient. The fact that the largest average outflow speeds in the penumbra ($>5 \text{ km s}^{-1}$) stand out toward the outer penumbra (see radial velocity profile of the outflows in Figure 4) might be partly due to a larger fill factor of outflows in the outer penumbra that dominates the average. According to our results, the overall picture is that of an NEF mainly driven by magneto-convection in the inner and middle penumbra, in agreement with the results of Rempel (2011).

Observational studies of sunspots have shown that the penumbral filaments carrying the NEF in penumbrae have well-defined “footpoints” at $\tau = 1$, see, e.g., Tiwari et al. (2013). The filaments footpoints are seen to confine the upflows (sources) and the downflows (sinks) associated with the Evershed flow in the penumbra, separately. This is an important difference in these simulations, given that the upflow cell covers a large portion of the NEF filaments, meaning that almost the entire filaments behave as a “footpoint.” However, the lack of information on a true geometrical height scale in the current observational analysis techniques makes the comparison of numerical models with the highest-resolution observations very challenging, unless the simulations include the computation of the observational quantities using radiative transfer computations (forward computations).

Overall, our analysis of the NEF essentially reinforces conclusions of Scharmer et al. (2008), Rempel et al. (2009a), and Rempel (2011) stating that the penumbra is dominated by anisotropic magnetoconvection and that the NEF can be understood as the convective flow component in the direction of the magnetic field, i.e., the overall underlying energy source is convective instability.

Unlike the NEF, the driving of the CEF occurs mainly in the middle and outer penumbra, and the footpoints (sources and sinks) of the CEF-carrying filaments are generally well-separated from each other. Furthermore, the upflow cells in the CEF-carrying filaments are less spread out compared to the NEF, i.e., less elongated in the radial direction, which enhances the role of the radial pressure gradients and allows for the existence of siphon-like inflows along field lines that connect to the inner penumbra.

In addition to the radial pressure gradients, the CEF is also affected by the inclined field of the penumbra, in a way similar to how the NEF is—i.e., the radial Lorentz force plays an important role in the driving of the CEFs. The combination of both radial forces results in fast inflows ($>5 \text{ km s}^{-1}$ on average)

near the $\tau = 1$ level. We found that, irrespective of whether the sources of the CEF are located in the middle or outer penumbra, the upflowing gas suffers a reduction of the vertical magnetic field combined with an enhancement of the radial field component. This leads to a positive contribution of the radial Lorentz force for the driving of the CEF.

Nonetheless, the energy conversion associated with the radial Lorentz force is, on average, smaller in the CEF sources than in the NEF sources, given that the magnetic field is, on average, weaker in the outer penumbra than in the inner penumbra. At first glance, this would imply a smaller radial acceleration of the CEF compared to the NEF. However, it is generally the sum of both the radial pressure force and radial Lorentz force that determines the radial acceleration of the CEF. Consequently, the inward acceleration of the fluid can eventually become even larger than that of the NEF. This occurs at several stages of the evolution of the CEF in the analyzed simulation. However, during the 10 hr analyzed in these simulations, the CEF shows up as a highly variable and unstable flow, while the NEF appears as a quasi-stationary and more robust feature in the penumbra.

Both the CEF and the NEF are strongly magnetized, and both are driven within a thin boundary layer close to $\tau = 1$. There are also other, smaller-scale flows (outflows and inflows) in the penumbra that are unrelated to the filamentary penumbra. In particular, the additional inflows are mostly driven by pressure gradients in regions with an (on average) opposed contribution of the radial Lorentz term, the latter of which favors outflows. This could explain why these inflows are of much smaller scales than the CEF.

According to observational studies, CEFs can occur under different physical circumstances. On the one hand, those CEFs that have been observed during the early stages of penumbra formation (e.g., Schlichenmaier et al. 2012; Romano et al. 2014; Murabito et al. 2016) usually appear as elongated patches at the outer edge of the proto-spot, and are unrelated to any filamentary structure because they are observed when the latter is not yet developed. Furthermore, the newly formed penumbral filaments host an NEF soon after their formation. Therefore, those inflows observed around forming sunspots may involve different physical driving mechanisms because they are essentially different to the CEFs studied in this simulation. A possible scenario is that they are driven only by gas pressure gradients that are caused by the increase of the magnetic field strength in the proto-spot.

On the other hand, the CEFs that have been observed (albeit more rarely) in well-developed penumbrae (Kleint & Sainz Dalda 2013; Louis et al. 2014; Siu-Tapia et al. 2017) share important similarities with the CEFs in the present simulations: they were observed either along singular penumbral filaments or, as in Siu-Tapia et al. (2017), along an array of penumbral filaments covering a sizable part of the penumbra in a mature spot, but with most of the penumbra still displaying the NEF as in our present simulation. This occurs in all three above-mentioned reported observations of CEFs in well-developed penumbrae. However, due to the lack of knowledge regarding the true geometrical height scale in the observations and the inability to measure vertical gradients below the photosphere, none of these works could determine the dominant forces driving the flows.

In particular, Siu-Tapia et al. (2017) reported the observation of a prominent CEF with lifetimes of ~ 2 days at photospheric

heights. Similarly to the simulations analyzed here, the CEF in those observations showed an associated filamentary structure, with the sources of the CEF (hot upflows in vertical field regions) identified in the outer penumbra and the sinks (cooler downflows in strong vertical field regions) at the inner penumbral boundary. Furthermore, we found that the general magnetic, thermal, and velocity structure along the central axes of the CEF-carrying filaments at $\tau = 1$ are remarkably similar to those reported in that work. Of particular interest is their finding of an enhanced temperature at the sinks of the CEF with respect to the surrounding environment and a very large field strengthening associated to supersonic downflow speeds. We also see these two aspects at the sinks of the CEF in the simulations. On the one hand, we found that deceleration takes place in the form of shocks at the sinks of both CEF- and NEF-carrying filaments. This can explain the local temperature rise found at their sinks. On the other hand, we found enhanced field strengths at the sinks of both CEF and NEF, reaching respective values up to ~ 5 kG and ~ 2.5 kG. The very low density of the downflowing gas produces the depression of the local $\tau = 1$ level at the sinks of both NEF and CEF. At the CEF sinks, the $\tau = 1$ depression, combined with the influence of the umbral field, contributes to the observation of such strong fields at those places; while at the NEF sinks, the local enhancement of the field is the result of the $\tau = 1$ depression combined with a net magnetic field intensification that is well-localized in height and might be produced by the supersonic downdrafts of magnetic flux at the outer penumbra, as proposed by van Noort et al. (2013).

The CEF in these simulations persists up to ~ 10 hr, which is much shorter than the lifetimes reported by Siu-Tapia et al. (2017), although the feature studied by Siu-Tapia et al. (2017) was extraordinary in comparison to other observed CEF events (see e.g., Kleint & Sainz Dalda 2013; Louis et al. 2014). However, in both cases, the CEFs have much shorter lifetimes than the NEFs and can be thought of as transitory events relative to the latter. Furthermore, similarly to what happens in these simulations, Siu-Tapia et al. (2017) reported that the penumbral sector harboring the CEF displays only an NEF after the CEF disappears. We have not studied the exact mechanism of how the CEF is reversed to an NEF. However, a negative contribution of the radial Lorentz term, combined with a strong reduction of the radial pressure gradient at the sources of the CEF, would strongly favor the driving of outflows instead. A physical mechanism leading to the change of the magnetic field configuration and of the plasma conditions in the penumbra in such a way would likely involve magnetic reconnection.

Our analysis of the driving forces of the CEF in the simulated penumbra clearly shows that the CEF is a siphon flow driven by pressure gradients along the penumbral filaments. The inclined field in the penumbral filaments causes the radial Lorentz force to also play an important role in accelerating the gas inward. Furthermore, apart from the most prominent and persistent groups of CEF-carrying filaments during the analyzed temporal interval (e.g., those shown in Figure 2 and the portion analyzed in Figures 7 and 9), there are also a few other shorter-lived, CEF-carrying filaments that appear intermittently at different azimuths in the penumbra. We do not discard the possibility that CEFs may actually occur along penumbral filaments more regularly than observed, but their short lifetimes prevents them being easily observed.





According to our results, that would occur whenever a significant pressure gradient favoring CEFs is established in a penumbral filament, as in those cases in which the outer footpoint of the filament is not strengthened with respect to the inner footpoint (see, e.g., the CEF-carrying filament shown in Figure 3). Alternatively, CEFs may also appear as a consequence of ongoing magnetic flux emergence in the penumbra. This interpretation was presented by Chen et al. (2017). In their recent MHD simulation, more than 60% of the simulated penumbra is dominated by CEFs that result from the mass drain into the umbra-penumbral boundary along the newly emerged field lines that coalesce and contribute to the horizontal field in the penumbra.

Nonetheless, there are very few reported observations of CEFs in well-developed sunspot penumbrae (Kleint & Sainz Dalda 2013; Louis et al. 2014; Siu-Tapia et al. 2017). This could also be due to a combination of their rare occurrence and short lifetimes. However, more theoretical studies on this topic, as well as high-temporal-cadence spectropolarimetric observations, are necessary to investigate the true occurrence frequency and learn more about the nature of CEFs in well-developed sunspot penumbrae—as well as their possible influence on the upper atmosphere.

The IEF in the uppermost part of the simulation box is a robust feature and the question of an IEF-CEF connection is compelling. However, the IEF shown in the simulation is possibly affected by the proximity of that flow to the top boundary, as well as by Alfvén speed reduction. This will be addressed when improved simulations become available.

We would like to thank the referee of this paper for providing insightful and very useful comments that improved our manuscript. This work was carried out in the framework of the International Max Planck Research School (IMPRS) for Solar System Science at the Max Planck Institute for Solar System Research (MPS). It is supported by the Max Planck Society and by BECAS CONACyT AL EXTRANJERO 2014. This work was partly supported by the ERC under grant agreement No. 695075, and the BK21 plus program through the National Research Foundation (NRF) funded by the Ministry of Education of Korea. The National Center for Atmospheric Research is sponsored by the National Science Foundation.

ORCID iDs

A. L. Siu-Tapia  <https://orcid.org/0000-0003-0175-6232>
 M. Rempel  <https://orcid.org/0000-0001-5850-3119>
 A. Lagg  <https://orcid.org/0000-0003-1459-7074>
 S. K. Solanki  <https://orcid.org/0000-0002-3418-8449>

References

- Bellot Rubio, L. R. 2010, *The Evershed Flow and the Brightness of the Penumbra* (Berlin: Springer), 193
 Bellot Rubio, L. R., Balthasar, H., & Collados, M. 2004, *A&A*, **427**, 319
 Borrero, J. M. 2009, *ScChG*, **52**, 1670
 Borrero, J. M., & Ichimoto, K. 2011, *LRSP*, **8**, 4
 Borrero, J. M., Lagg, A., Solanki, S. K., & Collados, M. 2005, *A&A*, **436**, 333
 Brummell, N. H., Tobias, S. M., Thomas, J. H., & Weiss, N. O. 2008, *ApJ*, **686**, 1454
 Chen, F., Rempel, M., & Fan, Y. 2017, *ApJ*, **846**, 149
 Choudhuri, A. R. 1986, *ApJ*, **302**, 809
 Clyne, J., Mininni, P., Norton, A., & Rast, M. 2007, *NJPh*, **9**, 301
 Clyne, J., & Rast, M. 2005, *Proc. SPIE*, **5669**, 284

- Danielson, R. E. 1961, *ApJ*, 134, 289
- del Toro Iniesta, J. C., Bellot Rubio, L. R., & Collados, M. 2001, *ApJ*, 549, L139
- Dialetis, D., Mein, P., & Alissandrakis, C. E. 1985, *A&A*, 147, 93
- Evershed, J. 1909, *MNRAS*, 69, 454
- Heinemann, T., Nordlund, A., Scharmer, G. B., & Spruit, H. C. 2007, *ApJ*, 669, 1390
- Kitiashvili, I. N., Kosovichev, A. G., Wray, A. A., & Mansour, N. N. 2009, *ApJL*, 700, L178
- Kleint, L., & Sainz Dalda, A. 2013, *ApJ*, 770, 74
- Louis, R. E., Beck, C., Mathew, S. K., & Venkatakrishnan, P. 2014, *A&A*, 570, A92
- Meyer, F., & Schmidt, H. U. 1968, *Angew. Math. Mech.*, 48, 218
- Montesinos, B., & Thomas, J. H. 1997, *Natur*, 390, 485
- Murabito, M., Romano, P., Guglielmino, S. L., Zuccarello, F., & Solanki, S. K. 2016, *ApJ*, 825, 75
- Rempel, M. 2011, *ApJ*, 729, 5
- Rempel, M. 2012, *ApJ*, 750, 62
- Rempel, M. 2014, *ApJ*, 789, 132
- Rempel, M. 2015, *ApJ*, 814, 125
- Rempel, M., & Schlichenmaier, R. 2011, *LRSP*, 8, 3
- Rempel, M., Schüssler, M., Cameron, R. H., & Knölker, M. 2009a, *Sci*, 325, 171
- Rempel, M., Schüssler, M., & Knölker, M. 2009b, *ApJ*, 691, 640
- Romano, P., Guglielmino, S. L., Cristaldi, A., et al. 2014, *ApJ*, 784, 10
- Scharmer, G. B. 2009, *SSRv*, 144, 229
- Scharmer, G. B., Nordlund, A., & Heinemann, T. 2008, *ApJL*, 677, L149
- Scharmer, G. B., & Spruit, H. C. 2006, *A&A*, 460, 605
- Schlichenmaier, R. 2009, *SSRv*, 144, 213
- Schlichenmaier, R., Jahn, K., & Schmidt, H. U. 1998a, *ApJ*, 493, L121
- Schlichenmaier, R., Jahn, K., & Schmidt, H. U. 1998b, *A&A*, 337, 897
- Schlichenmaier, R., Rezaei, R., & González, N. 2012, in ASP Conf. Ser. 455, 4th Hinode Science Meeting: Unsolved Problems and Recent Insights, ed. L. R. Bellot Rubio et al. (San Francisco, CA: ASP), 61
- Siu-Tapia, A. L., Solanki, S. K., Lagg, A., van Noort, M., & Jurčák, J. 2017, *A&A*, 607, A36
- Solanki, S. K. 2003, *A&AR*, 11, 153
- Solanki, S. K., & Montavon, C. A. P. 1993, *A&A*, 275, 283
- Spruit, H. C., & Scharmer, G. B. 2006, *A&A*, 447, 343
- Thomas, J. H., & Montesinos, B. 1993, *ApJ*, 407, 398
- Thomas, J. H., & Weiss, N. O. (ed.) 1992, in Proc. NATO Advanced Research Workshop on the Theory of Sunspots, Sunspots: Theory and observations, ed. J. H. Thomas & N. O. Weiss (Cambridge: Kluwer), 438
- Thomas, J. H., & Weiss, N. O. 2004, *ARA&A*, 42, 517
- Thomas, J. H., & Weiss, N. O. 2008, Sunspots and Starspots (Cambridge: Cambridge Univ. Press)
- Thomas, J. H., Weiss, N. O., Tobias, S. M., & Brummell, N. H. 2002, *Natur*, 420, 390
- Tiwari, S. K., van Noort, M., Lagg, A., & Solanki, S. K. 2013, *A&A*, 557, A25
- Tritschler, A. 2009, in ASP Conf. Ser. 415, The Second Hinode Science Meeting: Beyond Discovery-Toward Understanding, ed. B. Lites et al. (San Francisco, CA: ASP), 339
- van Noort, M., Lagg, A., Tiwari, S. K., & Solanki, S. K. 2013, *A&A*, 557, A24
- Vögler, A., Shelyag, S., Schüssler, M., et al. 2005, *A&A*, 429, 335
- Wiehr, E. 1995, *A&A*, 298, L17